

Deformation of *Top-Down* and *Bottom-Up* Silver Nanowires

Austin M. Leach

Graduate Research Assistant

School of Materials Science and Engineering, Georgia Institute of Technology

Matt McDowell

Undergraduate Research Assistant

School of Materials Science and Engineering, Georgia Institute of Technology

Ken Gall

Associate Professor

School of Materials Science and Engineering, Georgia Institute of Technology

George Woodruff School of Mechanical Engineering, Georgia Institute of Technology

Abstract

We employ atomistic simulations to probe the deformation behavior of experimentally observed *top-down* and *bottom-up* FCC silver nanowires. We consider stable, $\langle 110 \rangle$ oriented nanowires with a rhombic and truncated-rhombic cross section, representative of *top-down* geometries, as well as the multiply twinned pentagonal nanowire that is commonly fabricated in a *bottom-up* approach. We simulate the tensile deformation from a stable, experimentally observed structure to failure for each nanowire structure. A detailed, mechanistic explanation of the initial defect nucleation is provided for each nanowire. The three geometries are shown to exhibit different levels of strength and to deform by a range of mechanisms depending on the nanowire structure. In particular, the deformation behavior of *top-down* and *bottom-up* nanowires is shown to be fundamentally different. The yield strength of nanowires ranging from 1-25 nanometers in diameter is provided and reveals that in addition to cross sectional diameter, the strength of nanowires is strongly tied to the structure. This study demonstrates that nanowire structure and size may be tailored for specific mechanical requirements in nanometer scale devices.

Keywords: nanowires, nanorods, mechanical behavior, pentagonal, molecular dynamics simulations, nanomechanics

1. Introduction

Nanowires are discernable by the geometry of their cross sections. In turn, this geometry is a manifestation of how the nanowires were created and the mechanisms by which the wires attained a state of minimum free energy. In general, nanowires may be separated into two classes based on the method of fabrication: *top-down* and *bottom-up*. *Top-down* methods involve extraction of a nanowire from a bulk sample through processes such as electron beam lithography or mechanical reduction,^[1-4] while *bottom-up* classifies nanowires that have been grown through chemical or molecular assembly or by template assisted electrodeposition.^[5-13] For further information on these processes, the reader is referred to thorough reviews of current methodologies for the fabrication of one-dimensional nanostructures.^[14-16]

When subjected to an applied stress, bulk and nanometer scale materials exhibit fundamentally different mechanical responses. For instance, consider the tensile behavior of monolithic metals (single crystal and unalloyed) at two different length scales portrayed in Figure 1. Bulk material mechanical response is typified by linear-elastic deformation followed by yield and subsequent plastic flow, generally not exceeding the MPa range.^[17] However, at nanometer scales, strengths in the GPa range are attainable and the overall response is characterized by a series of discrete yielding events leading to fracture.^[18-20] The quantized nature of

deformation at the nanometer scale reveals a disparity in the loading method. If the applied tensile stress is incrementally increased during deformation (force control), the mechanical response exhibits instabilities in strain corresponding to ‘instantaneous’ changes in specimen length due to the motion of internal defects. Conversely, applying an incrementally

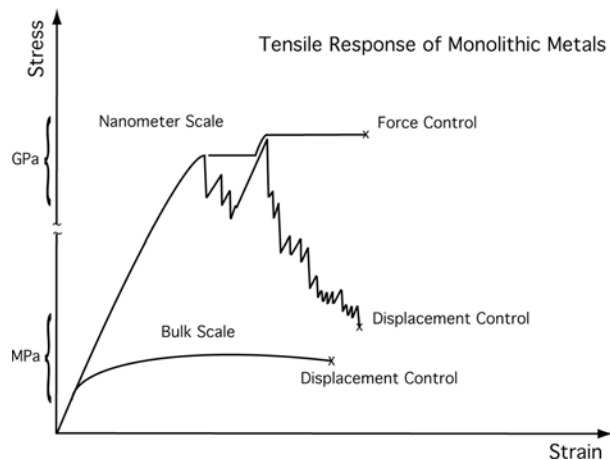


Figure 1. Schematic of the mechanical response of bulk and nanometer scale monolithic metals under force and displacement controlled tensile loading.

increasing strain (displacement control) reveals yielding in increments of force (stress) instability attributable to dissipation of stored strain energy through the nucleation and motion of internal defects.

The complexities associated with experimental measurements of the mechanical properties of nanometer scale materials preclude conventional testing methods and lend towards computational tools to simulate the mechanical behavior using atomistic simulations, specifically, molecular dynamics (MD). MD simulations using the embedded atom method (EAM) have provided a fundamental understanding of the mechanical behavior of nanowires.^[21-35]

In particular, nanowires of face-centered-cubic (FCC) metals have been studied extensively. Simulations of gold nanowires^[21] have shown that surface-stress resulting from excess energy at free surfaces can be sufficient to induce a phase transformation from FCC to body-centered-tetragonal if the wire cross-section is reduced to a critical dimension. Recently it has been demonstrated that surface stresses may also facilitate reversible lattice reorientations in some FCC nanowires, leading to shape-memory and pseudoelastic behavior.^[29-33] In general, single crystal metallic nanowires are predicted to deform by two deformation mechanisms, twinning and partial dislocation motion (slip).^[34] It has been shown that the initial deformation mechanism is dependent not only on the nanowire axial and free surface orientations (in relation to the loading direction), but also on the predictive capacity of the atomistic model with respect to the unstable and intrinsic stacking-fault energies.^[35, 36]

Thus far, MD simulations of the deformation of metallic nanowires have primarily focused on wire geometries that are inherently unstable due to high-energy surface and axial orientations. A notable exception is the recent work by Hyde *et al.*,^[27] on single-crystal gold nanowire structures; this study investigates the mechanical properties of stable $\langle 110 \rangle$ and $\langle 111 \rangle$ axial orientations, but considers the more hypothetical, circular cross-sectional geometries rather than experimentally observed nanowire geometries (which are typically faceted). While these investigations have been crucial in formulating an initial understanding of nanowire mechanical behavior, the scope of their practical application to the structural integrity of nanometer scale devices may be limited as the simulated nanowire configurations are mostly theoretical. We also note that the mechanical response of nanowires with a rhombic cross-section has been previously considered^[22, 29-34]. However, these studies have focused primarily on reversible deformation paths which lead to shape memory and pseudoelastic behavior. The deformation behavior of the truncated-rhombic nanowires, to the author's knowledge, has not been considered.

We consider $\langle 110 \rangle$ axially oriented silver nanowires of rhombic and truncated-rhombic geometries, representative of *top-down* fabrication; and also the multiply twinned, pentagonal geometry typifying a *bottom-up* fabrication route. The rhombic structure was first observed in high-resolution transmission electron microscopy (HRTEM) by Kondo and Takayanagi^[4] and later by Kizuka^[37] and Rodrigues *et al.*^[38] in gold nanowires created from electron-beam irradiation of thin films. The cross-sectional geometry is a result of the crystallography of four low-energy $\{111\}$ side surfaces that join to form a rhombus. A truncation of the acute vertices of the rhombic nanowires results in the exposure of $\{100\}$

surfaces along the nanowire length and a truncated-rhombic geometry. The truncated-rhombic nanowires are predicted to be energetically more favorable than the rhombic structure^[39] and have been specifically observed during *in-situ* HRTEM observation of *top-down* nanowire fabrication in silver.^[40, 41] The pentagonal geometry is a stable structure produced by chemical growth using techniques utilized by Caswell *et al.*^[5] as well as Sun and Xia^[11] for silver nanowires. The pentagonal nanowire structure has been extensively characterized using electron microscopy and electron diffraction,^[7, 42-46] but the deformation behavior has not been investigated using MD, particularly in the case of silver. An excellent discussion of the energetics and relative stability of the three nanowires is found in the work by Tommei *et al.*^[39]

In this study, we present a detailed analysis of the mechanical behavior of experimentally observed, inherently stable *top-down* and *bottom-up* silver nanowires. We probe the mechanical behavior of the nanowires under tension from an equilibrium configuration until failure with specific emphasis on the mechanisms of initial yield. We consider nanowires ranging from 1 – 25 nanometers in diameter (up to two million atoms). The consideration of large nanowires broadens the scope of the research to more commonly observed and fabricated nanowire sizes. We show that the method of fabrication (*top-down* vs. *bottom-up*) has a direct influence on the mechanical behavior of metallic nanowires. While we only simulate the deformation of silver nanowires, nanowires fabricated from other low stacking-fault energy metals such as gold and copper are expected to show similar behavior. We illustrate that *top-down* and *bottom-up* nanowire structures demonstrate fundamentally different deformation mechanisms and dissimilar overall mechanical behavior.

Our results also indicate a strong, geometry dependent size effect on the tensile yield strength. Several researchers have described a size effect in the elastic properties of nanometer scale materials, in experiments,^[47-50] continuum based models,^[51-55] and atomistic simulations.^[24, 56] In all cases, the variation of the elastic properties is attributable to the increasing influence of surfaces as the dimensions of the structure are reduced. In this sense, our findings reaffirm the former conclusion, that the excess energy of free surfaces has a significant influence on the mechanical behavior of nanowires; however, our results are distinct in that we observe the size effect in the plastic regime. Furthermore, we demonstrate that in relation to the bulk mechanical properties, the magnitude of the size effect is different for nanowires of the same material and axial orientation but of varying geometry.

The paper is organized in the following manner. We first present an overview of the tensile deformation from zero strain to failure including a thorough discussion of the initial defect nucleation, for each nanowire geometry. We then offer conclusions on the mechanical behavior of metallic nanowires. Lastly, the methods employed to simulate the deformation of the silver nanowires are described and a detailed presentation of the crystallographic structure of the three considered geometries is provided.

2. Results

The tensile stress-strain response of the rhombic, truncated-rhombic, and pentagonal nanowires is presented in

Figure 2. The response is provided from zero-strain to failure for each nanowire. The three-nanowire geometries show similar mechanical behavior up to the onset of plastic deformation, characterized by an initial nonlinear elastic response. However, after the primary defect nucleation event, the mechanical response of the three nanowires is fundamentally different; each undergoing deformation by

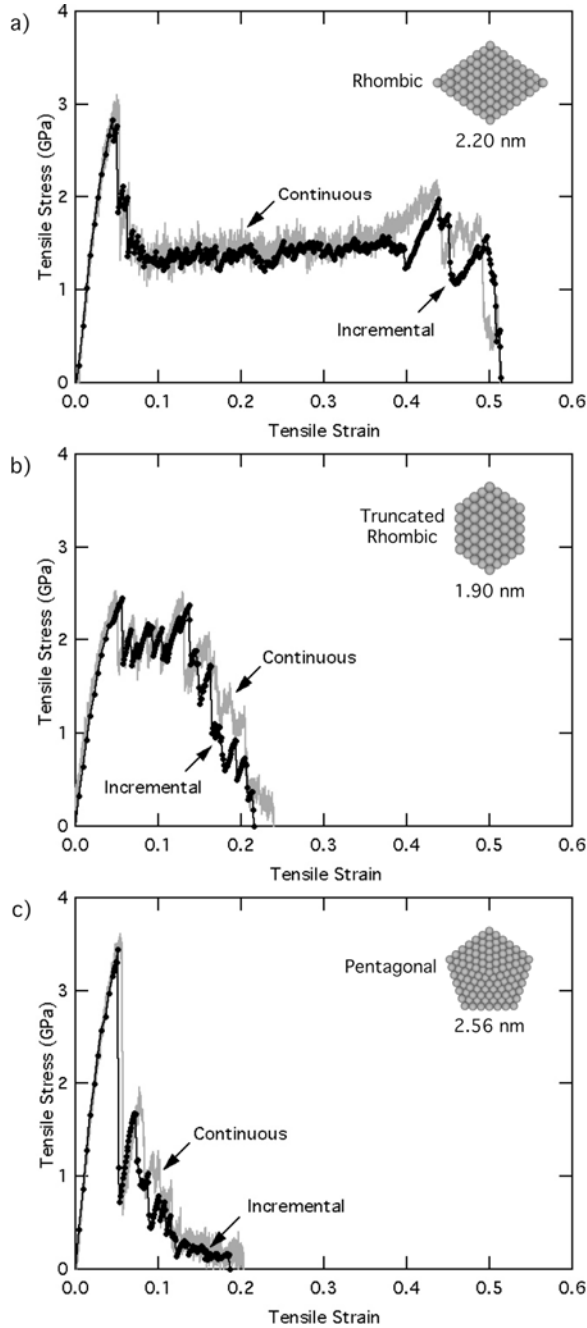


Figure 2. Stress-strain response of *top-down* (a,b) and *bottom-up* (c) silver nanowires. The nanowire geometry and diameter are indicated for each response. The wires were loaded in tension from an unstrained, thermally equilibrated (300 K) configuration to failure. The stress shown is the virial stress.

means of a different mechanism leading to vastly different failure strains. In the following, we provide a detailed presentation of the mechanical response of the three nanowires. Snapshots representative of the dominant stages of overall deformation for each nanowire are provided with a particular focus on the mechanisms surrounding initial yield.

2.1 Top-Down Rhombic Silver Nanowires

The mechanical response of a rhombic silver nanowire is presented in Figure 2a. Snapshots of the nanowire at consecutive stages of deformation are shown in Figure 3. The defect free, minimum energy configuration (Figure 3a) sustains an axial stress of approximately 3 GPa before partial dislocations of the Shockley type are heterogeneously nucleated at the intersection of two $\{111\}$ free surfaces, resulting in the formation of an intrinsic stacking fault in the FCC lattice. The nanowire then undergoes deformation twinning, where coherent twin boundaries are propagated from the initial stacking fault to the nanowire ends (Figure 3b-c). During this process, the wire undergoes an axial lattice reorientation from $\langle 110 \rangle$ to $\langle 100 \rangle$ resulting in the conversion of the low-energy $\{111\}$ free surfaces to higher-energy $\{100\}$ surfaces. As a direct consequence of the free surface orientation, the cross-sectional geometry transitions from

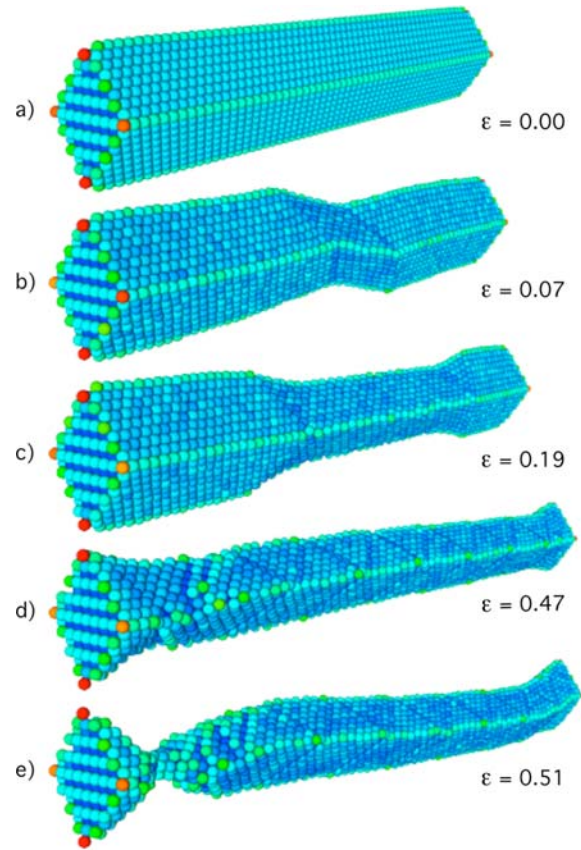


Figure 3. Snapshots of a rhombic silver nanowire during tensile deformation at 300 K. The strain value for each snapshot is indicated and corresponds to the stress-strain response in Figure 2a.

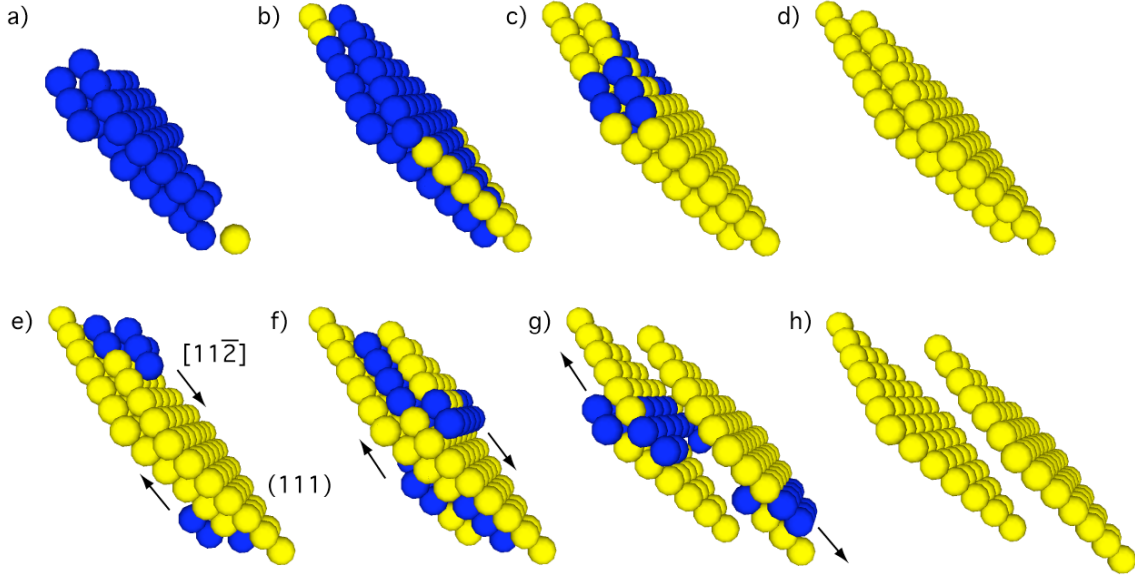


Figure 4. Stacking fault formation (a-d) and twin propagation (e-h) in a rhombic silver nanowire subjected to tensile deformation at 10 K. Atoms are colored by a centrosymmetry parameter indicating the degree of coordination for each atom relative to its undisturbed (bulk) position. Blue atoms correspond to partial dislocations while yellow atoms are representative of stacking fault coordination. Fully coordinated atoms are not shown. Arrows are shown indicating the direction of partial dislocation motion during the propagation of the twin boundaries.

rhombic to rectangular during the twinning process. The nanowire expands an extraordinary amount, over 40% of its original length during the reorientation. The reoriented $\langle 100 \rangle$ nanowire is essentially defect-free; the twin boundaries are pinned at the free ends due to the imposed boundary conditions. The $\langle 100 \rangle$ nanowire then behaves elastically followed by yield through the nucleation and motion of additional Shockley partial dislocations (Figure 3d). The plastic flow is restricted as the partials form a network of Lomer-Cottrell locks along the nanowire length. Finally, the nanowire deforms into a helically arranged cylindrical structure as the cross-section is reduced through necking (Figure 3e), eventually leading to the formation of a single atomic strand just prior to failure.

The initial decrease in strength of the rhombic nanowire is a result of the free surface induced heterogeneous nucleation of partial dislocations. Figure 4 provides a detailed account of the partial dislocation nucleation and the subsequent twinning process. The first partial dislocation nucleates at a large-angle vertex of the rhombic cross section as apparent in Figure 4a. The partial traverses the cross-section of the nanowire along a $\{111\}$ slip plane and in doing so creates an intrinsic stacking fault in the FCC lattice (Figure 4a-d). The deformation continues through defect-assisted deformation twinning where the stacking fault serves as a twin nucleus. In the deformation twinning process, partial dislocations nucleate at the low-angle vertex of the rhombic cross-section on adjacent $\{111\}$ planes of the stacking fault at opposite ends, and propagate in a $\langle 112 \rangle$ direction, following the classical $\{111\}\langle 112 \rangle$ twinning system of the FCC lattice (Figure 4e-h). When the partials have swept the $\{111\}$ plane and reached the free surface, this process is repeated. The motion of the partial dislocations serves to advance the coherent twin boundaries along the nanowire length, and in

the process, restores the FCC stacking sequence through the aforementioned lattice reorientation.

2.2 Top-Down Truncated-Rhombic Silver Nanowires

The experimentally observed truncated-rhombic geometry demonstrates promising mechanical integrity for nanometer scale devices due to the small difference between the yield stress and the stress sustained during plastic flow. The nanowire retains nearly 75% of its strength for over half of the total strain-to-failure. The stress-strain response is presented in Figure 2b, while the snapshots of deformation are shown in Figure 5. As in the case of the rhombic nanowire, plastic deformation is facilitated by the nucleation of partial dislocations leading to the formation of a stacking fault. However, the truncated-rhombic nanowire does not undergo deformation twinning; instead, the deformation is constrained to the motion of more isolated partial dislocations. The dislocations move in a ‘stair-rod’ fashion, leaving behind a network of stacking faults in the nanowire, similar to the deformation substructure observed in the reoriented rhombic nanowire at much larger strain (Figure 3d). The stair-rod structure is first observed in the middle region of the nanowire (Figure 5b), and with increasing strain the network expands along the entire length of the nanowire (Figure 5c). The limited cross sectional area of the nanowire combined with the stair-rod stacking fault structure confines the subsequent nucleation and motion of additional dislocations to a localized region. As a result, the nanowire begins to dissipate the accumulated strain energy through necking as displayed in Figure 5d.

The mechanism responsible for incipient plasticity in the truncated-rhombic nanowires is the nucleation and motion of Shockley partial dislocations. The first partial dislocations

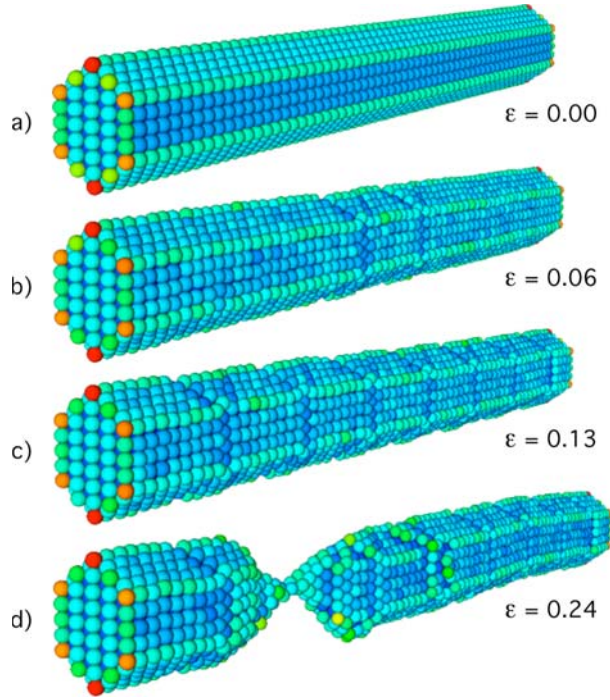


Figure 5. Snapshots of a truncated-rhombic silver nanowire during tensile deformation at 300 K. The strain value for each snapshot is indicated and corresponds to the stress-strain response in Figure 2b.

are heterogeneously nucleated at the intersection of a $\{100\}$ and $\{111\}$ free surface of the nanowire and create a stacking fault as they move through the cross-section (Figure 6a-c). Next, partial dislocations are nucleated at the intersection of the initial stacking fault and the $\{100\}$ surface (Figure 6d),

forming additional stacking faults in the previously mentioned stair-rod structure. The deformation then takes a path different than the rhombic nanowire. Deformation twinning begins via the nucleation and propagation of partial dislocations adjacent to the initial stacking fault, but is prevented as the partial dislocations are blocked by the stacking fault formed previously as part of the stair-rod structure (Figure 6e,f). These partial dislocations recede (Figure 6g), leaving a dislocation free stacking fault structure along the length of the nanowire (Figure 6h). Consequently, the truncated-rhombic nanowires show limited plastic flow and fracture at a much lower strain than the rhombic wires, which experienced very large strain enabled by deformation twinning.

2.3 Bottom-Up Pentagonal Silver Nanowires

The pentagonal nanowires possess the lowest cohesive energy of the three structures considered. The pentagonal structure is stabilized by internal twin boundaries that span the length of the nanowire. In addition to energetic stability, these twin boundaries provide an internal barrier to dislocation motion, which classically should result in high strength and low ductility. From the tensile response in Figure 2c, high strength is indeed observed. The pentagonal nanowires may be considered a multi-shell structure, consisting of concentrically stacked pentagonal shells. In this sense, the tensile deformation of the pentagonal wires may be easily described: deformation is initiated by fracture of the outer pentagonal shell at the intersection of two $\{100\}$ free surfaces. The fracture event is accompanied by a large decrease in axial stress; this results from the dissipation of accumulated elastic strain energy through the severing of electron-dense, nearest-neighbor metallic bonds. The outer shell fracture and the resulting deformation are illustrated in Figure 7. As apparent in Figure 7b, the outer

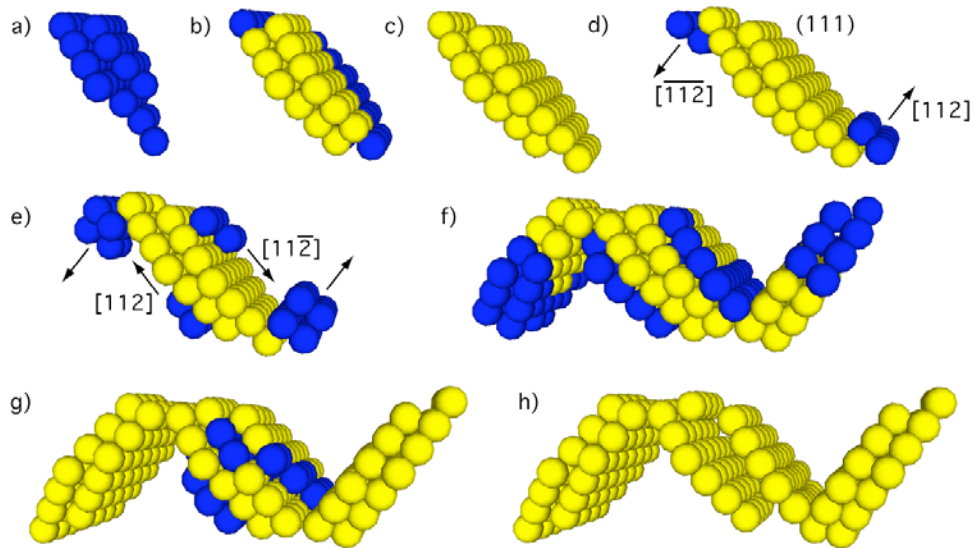


Figure 6. Stacking fault formation (a-c) and partial dislocation propagation (d-h) in a truncated-rhombic silver nanowire subjected to tensile deformation at 10 K. The atoms are colored as in Figure 4.

pentagonal shell fractures at several locations around the perimeter of the nanowire. Further deformation is achieved through the motion of dislocations within the vicinity of these fracture sites. Since the deformation is restricted to a small volume, the nanowire quickly begins to neck (Figure 7c), and with further applied strain a stable two atomic-strand nanobridge is formed before final failure. Stable nanobridges longer than two atoms are not experimentally observed during the extension of $\langle 110 \rangle$ oriented *top-down* nanowires,^[41] which is consistent with the predictions herein; however, interestingly, we predict their occurrence for the extension of $\langle 110 \rangle$ pentagonal nanowires.

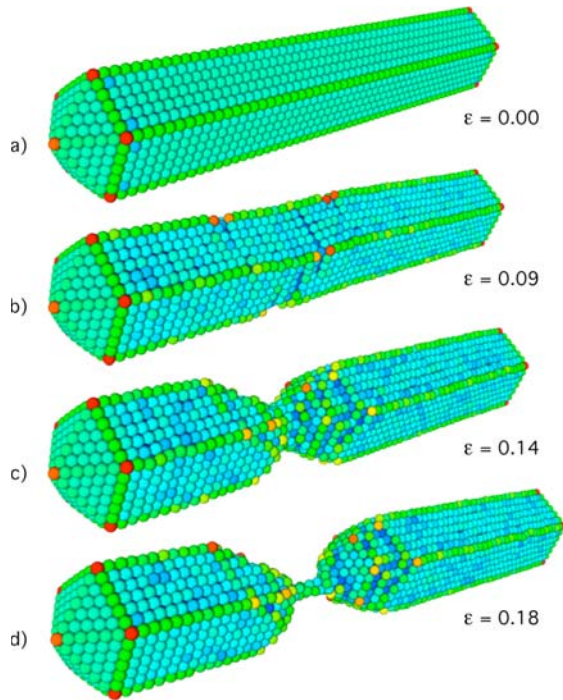


Figure 7. Snapshots of a pentagonal silver nanowire during tensile deformation at 300 K. The strain value for each snapshot is indicated and corresponds to the stress-strain response in Figure 2c.

The limited motion of partial dislocations within each wedge-shaped crystal of the nanowire characterizes the early deformation in the pentagonal nanowire. From the initial fracture location, Shockley partial dislocations are emitted and traverse a $\{111\}$ plane in a $\langle 112 \rangle$ direction until reaching an internal twin boundary, leaving behind a stacking fault in the process (Figure 8a-c). After reaching the twin boundary, the partial dislocation becomes immobilized thus causing an accumulation of energy which is then released through fracture at a new location on the outer shell (Figure 8d). This process continues until each wedge-shaped crystal is saturated with stacking faults, signifying complete circumferential fracture (Figure 8e-g). Complete circumferential fracture occurs at two locations along the nanowire length, separated by a finite distance. These circumferential fracture sites then bound the region in which further deformation occurs.

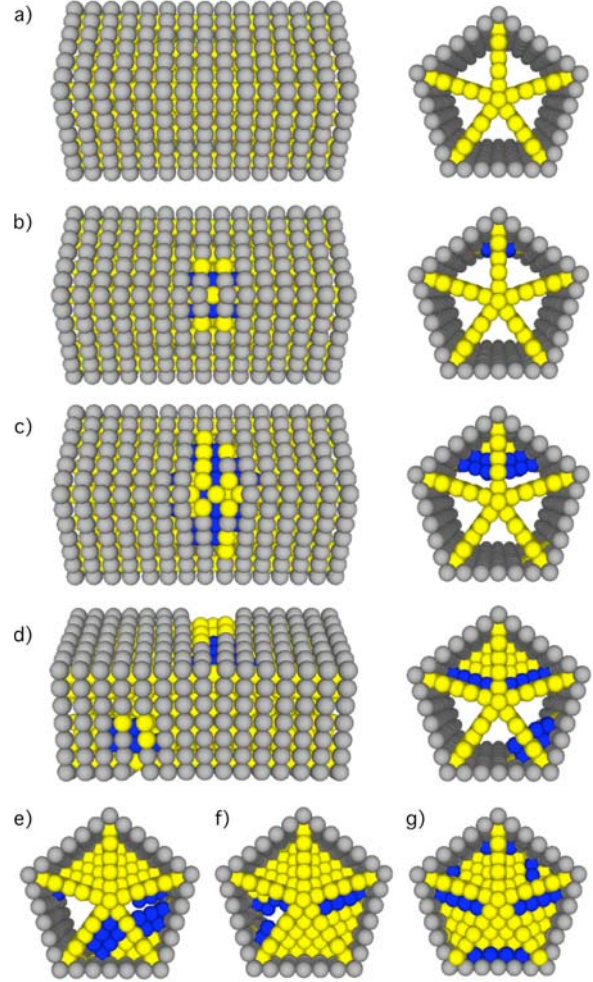


Figure 8. Outer shell fracture of a pentagonal silver nanowire (a-d) and corresponding partial dislocation nucleation (a-g) during tensile deformation at 10 K. A side view and a cross sectional view is shown for (a-d). Note that the wire is rotated in (d), showing fracture on the upper and lower surface of the wire. Complete circumferential fracture is evidenced through the defect structure in (e-f). The atoms are colored as in Figure 4; in addition, atoms with a surface coordination are shown in grey. The internal twin boundaries are colored yellow, as they have the same centrosymmetry as a stacking fault.

2.4 Size effect on yield strength

The tensile yield strength of the three nanowires is revealed to be strongly size and geometry dependent. For all three nanowire geometries, we observe decreasing yield strength with increasing nanowire diameter, as shown in Figure 9. The pentagonal nanowires provide the highest strength for all diameters considered, followed by the rhombic and truncated-rhombic geometries, respectively. Although, the magnitude of the yield strength is sensitive to the strain rate and also to the volume parameter used in the calculation of the virial stress, the relative strength of the three will not be affected by a change in these parameters. The size effect will be further discussed in the following section.

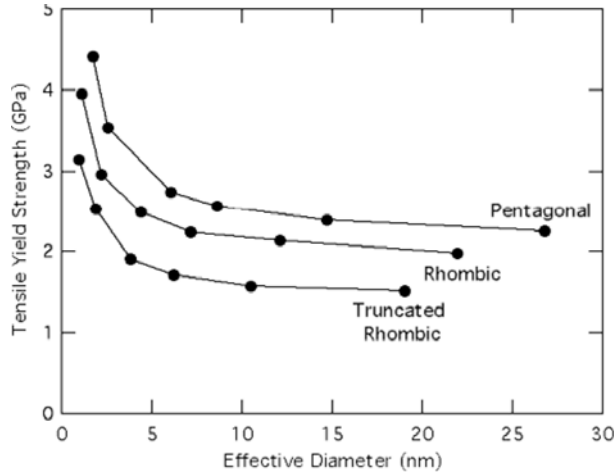


Figure 9. Size effect on the tensile yield strength of pentagonal, rhombic, and truncated-rhombic silver nanowires.

3. Discussion

Our results indicate that the mechanical behavior of energetically stable nanowires is strongly dependent on the cross-sectional geometry and surface orientation. Since the geometry and internal stability are directly linked to fabrication, we infer that the method of fabrication (*top-down* vs. *bottom-up*) has a dominant influence on mechanical strength and the mechanisms of deformation.

3.1 Top-Down Deformation Behavior

The total cohesive energy of a nanowire can be approximated as the summation of the contribution from atoms at free surfaces and the interior (non-surface) atoms. The local minimum energy configuration for an atom in an FCC lattice is to be surrounded by 12 nearest neighbors, each at an equivalent distance away. Surface energy is the consequence of this condition not being fully satisfied. The number of nearest neighbors is dependent on the atomic density of the surface being considered. For this reason, the magnitude of the surface energy is dependent on the surface orientation: for FCC materials, the close packed $\{111\}$ surfaces have the lowest surface energy, followed by $\{100\}$ and then $\{110\}$ type surfaces. In bulk materials, surfaces comprise a minimal portion of the total volume, and thus the surface energy contribution is minimal. In nanowires, free surfaces constitute a considerable portion of the total volume, and the effect of surface energy is no longer insignificant. Atoms at free surfaces will minimize their energy by contracting towards the interior of the nanowire to maximize their local atomic density. As a result, tensile surface stresses induce an intrinsic compressive stress in the nanowire interior. The extent to which this surface stress induced compressive stress influences nanowire stability depends on the axial orientation. For elastically soft axial orientations, (e.g. $\langle 100 \rangle$), the surface stress is capable of inducing structural transformations,^[21, 22] while for the stiffer $\langle 110 \rangle$

orientation, the influence of surface stress is less significant.

It has been previously noted that free surface orientation influences the operant deformation modes in metallic nanowires^[34] however, whether the influence is of an energetic or crystallographic origin is not fully understood. Since the truncated-rhombic nanowires differ from the rhombic ones only by free surface orientation, we perform a systematic comparison of the deformation observed in the two geometries in order to clarify the effect of surface orientation on mechanical behavior. The initial defect nucleation in both the rhombic and the truncated-rhombic nanowires results in the formation of an intrinsic stacking fault. After the formation of the first stacking fault, the deformation paths of the two-nanowire geometries deviate from a common path.

As presented previously, silver nanowires with a rhombic cross-section completely bounded by $\{111\}$ surfaces mechanically deform through deformation twinning. A defining characteristic of this type of deformation is the shape change produced during deformation. The shape change is restricted by the crystallography of the cross-section. For the rhombic nanowire, the shape change is evidenced through the conversion of the cross-section geometry from rhombic to rectangular during the $\{111\}\langle 110 \rangle$ to $\{100\}\langle 100 \rangle$ lattice reorientation. The $\{111\}$ free surface and $\langle 110 \rangle$ axial orientation of the rhombic nanowires creates an ideal crystallographic path for the shape change to occur thus allowing deformation twinning to control the mechanical response.

The truncated-rhombic nanowires were predicted to deform by the organized motion of partial dislocations, which form a 'stair-rod' structure along the nanowire length. The $\{100\}$ surfaces exposed from the truncation of the rhombic cross-section prevent the shape change that must be accommodated for deformation twinning to occur. We conducted simulations with varying levels of truncation to elucidate this effect. Interestingly, our results indicate that the likelihood of twinning as a mechanism of deformation is determined by the extent of truncation. Nanowires with a less severe truncation than those presented in Section 2.2 were observed to deform via competing mechanisms of twinning and slip. As the extent of truncation is reduced from that in Section 2.2 the propensity for twinning is increased. For the nanowires with a reduced truncation, the deformation twinning results in the transformation of $\{111\}$ surfaces to $\{100\}$ as in the case for the perfect rhombic wires, and interestingly, the $\{100\}$ surfaces of the truncated faces are reoriented to $\{110\}$, thus following the hierarchical order of surface energies for the FCC lattice ($E_{\{111\}} < E_{\{100\}} < E_{\{110\}}$).

The implication of these results is that the influence of surface orientation on twinning as a mode of deformation is primarily crystallographic. In order for twinning to be the operant mode of deformation, there must exist a minimum energy path to accommodate the shape change produced from the lattice reorientation. Clearly, truncating the rhombic nanowire alters the energetic landscape for deformation. While we cannot conclude the exact nature of the energetic barrier to deformation twinning in the truncated-rhombic nanowires, we can conclude the

following: with increasing truncation of the rhombic nanowire, it becomes more favorable to activate slip on a secondary system than to propagate the coherent interfaces of the initial stacking fault on the primary slip system. This topic is the focus of a future publication.

3.2 Bottom-Up Deformation Behavior

The prevailing structural feature of *bottom-up* nanowires is internal stability. Contrary to *top-down* nanowires, *bottom-up* structures maintain a stable atomic configuration during the fabrication process. Mechanically, this internal stability creates two effects: it provides a larger energetic barrier to defect formation and in the special case of the multiply twinned pentagonal nanowire, it limits ductility by hindering the motion of defects. The ensuing mechanical behavior is expected; the nanowires exhibit high strength and localized plastic deformation with a relatively low strain to failure.

The internal stability of the pentagonal nanowire arises from the five coherent twin boundaries that span the nanowire length. Similar to the *top-down* nanowires, the initial defect in the pentagonal nanowire is heterogeneously nucleated at the intersection of two external surfaces. In fact, the nucleation site may be considered as the intersection of the internal, coherent twin boundary with the free surface. In the *top-down* wires, the nucleated partial dislocations glide along the slip planes, undisturbed by internal planar defects. For a single crystal nanowire, the relation between the axial orientation and the loading direction determines the crystallographic slip systems that may be activated when a critical resolved shear stress is overcome: this is the basis of a Schmid factor analysis. Typically, this approach does not apply to polycrystalline materials; however, since each crystal in the pentagonal nanowire possesses a common $\langle 110 \rangle$ texture and span the length of the wire, the approach is acceptable. However, the pentagonal nanowires present a more complicated scenario, since the nucleation site is bisected by an internal twin boundary.

The distinguishing characteristic of the initial deformation in the pentagonal nanowires is the fracture of the outer pentagonal shell. We find that fracture as a mechanism of deformation is justified for two reasons. First, the internal twin boundary prevents the unimpeded dislocation motion is observed in the initial nucleation event in the *top-down* nanowires. Secondly, the twin boundary is aligned with the tensile axis, thus the boundary is experiencing the maximum possible tensile stress from the imposed loading conditions. Given that the stress state is maximized on the twin boundary, and the dislocation nucleation is impeded by the same twin boundary, the consequence is atomic separation (fracture), along the twin boundary. The limited ductility observed in the pentagonal wires results from the motion of the partial dislocations that are emitted during the fracture event. The motion of these partials is restricted by the internal twin boundaries, an additional strengthening mechanism arising from the internal stability.

3.3 Size Effect on Yield Strength

The magnitude of the yield strength of nanowires is controlled by two factors. First, the elastic modulus (stiffness) determines the rate of change of the tensile stress with strain in the nanowire and secondly, for a specific geometric configuration, a critical activation energy must be attained before a defect is nucleated in the nanowire. With respect to the first, if the yield strain is held constant, the yield strength will scale directly with the elastic modulus: a high stiffness will result in a higher yield strength than will a low stiffness, for an equivalent yield strain. The nucleation site in the nanowire determines at what strength the activation energy will be attained, and a defect will nucleate. For all three nanowires, we observe the nucleation at a corner formed at the intersection of two free surfaces. In essence, the corners act to locally magnify the stress state, thus controlling the stress required to attain the activation energy for defect nucleation. Accordingly, a variation in the elastic modulus or nucleation site will affect the magnitude of the yield strength.

To determine the dominant contribution to the yield strength size effect, we determined the elastic modulus for all nanowires from molecular statics calculations. The rhombic and truncated-rhombic nanowires show a nearly identical elastic modulus as a function of nanowire diameter, while the pentagonal nanowires are considerably stiffer over the same range of diameters. It is apparent, from Figure 9, that the pentagonal nanowires show the highest yield stress followed by the rhombic, then the truncated-rhombic nanowires. We conclude that the pentagonal nanowires exhibit higher yield strength primarily from the increased elastic modulus relative to the other nanowire geometries. Also, defect nucleation at a free surface corner in the pentagonal nanowires is inhibited by the internal twin boundaries. This raises the activation energy, and thus the strength required for defect nucleation increases. The difference between the yield strength of the rhombic and the truncated-rhombic is more concise. Since the rhombic and truncated-rhombic geometries have the same elastic modulus size dependence, the yield strength difference must be related to the nucleation event. Indeed, as discussed earlier, the nucleation site for the two nanowires is different. The nucleation site in the truncated-rhombic nanowires imparts a larger stress amplification than does the nucleation site in the rhombic nanowires, this results in a lower stress required to reach the activation energy for defect nucleation.

4. Conclusion

The deformation behavior of experimentally observed $\langle 110 \rangle$ oriented silver nanowire structures was determined using atomistic simulations. *Top-down* nanowires with rhombic and truncated-rhombic cross-sections and *bottom-up* nanowires with a multiply twinned, pentagonal structure were analyzed. The mechanical response from zero strain to failure was presented for each nanowire, and the mechanisms of deformation were discussed in detail.

The operant deformation mechanism was revealed to depend strongly on the structure of the nanowire. Rhombic

nanowires with {111} side surfaces were observed to deform by deformation twinning, and consequently deformed to over 40% strain before failure. The truncated-rhombic nanowires which possess {100} in addition to the {111} surfaces, deformed by forming a ‘stair-rod’ structure of stacking faults along the nanowire length, arising from the widespread motion of partial dislocations. The multi-shell pentagonal nanowires yielded by fracture of the outermost pentagonal shell.

We also presented a structure-dependent size effect on the tensile yield strength of the nanowires. The strength was observed to be inversely proportional to the nanowire diameter and to be strongly dependent on the geometry of the nanowire. The pentagonal structure demonstrated the highest strength of the three structures, which we credit to the enhanced stiffness and internal resistance to deformation provided by the internal twin boundaries of the nanowire. The difference in strength between the rhombic and truncated-rhombic nanowires is attributed to the variation in free surface configuration, which alters the initial defect nucleation event.

The overarching premise of this work is that metallic nanowires may be tailored to the mechanical requirements of a functional device based on structure.

5. Experimental

All of the MD simulations in this work were performed using the EAM.^[57, 58] In this model of atomic interaction, the total energy U of a system of N atoms is a summation over two terms, a classical pair interaction and a many-body, embedding energy term and is given as

$$U = \sum_i^N \left(F_i(\bar{\rho}_i) + \frac{1}{2} \sum_{\substack{i,j \\ i \neq j}}^N \phi_{ij}(R_{ij}) \right) \quad (1)$$

where, F_i is the energy required to embed an atom into the background electron density $\bar{\rho}_i$ at position i and ϕ_{ij} is the short-range pair interaction between atoms i and j separated by a distance R_{ij} . In the EAM, $\bar{\rho}_i$ is the spherically averaged atomic electron density. This scheme allows for the computation of sizeable systems while also capturing the subtleties of electron density variations at free surfaces. The EAM potential developed by Voter and Chen^[59] was utilized for the present study. The potential is a semi-empirical function fitted to experimentally determined properties of silver, as summarized in Table 1. The Sandia developed molecular dynamics code, Warp,^[60] was used for all simulations.

Experimentally observed silver nanowires representative of *top-down* and *bottom-up* fabrication were considered for the analysis. Three nanowire geometries were modeled, each of a <110> axial orientation. The three-nanowire structures are presented in Figure 10. The *top-down* nanowires exhibit rhombic (Figure 10a) and truncated-rhombic (Figure 10b) cross-sections, while the *bottom-up* structure exhibits a pentagonal (Figure 10c) cross-section. The three wires will be referred to as rhombic, truncated-rhombic, and pentagonal. The rhombic and truncated-

Table 1. Fitting parameters of the Voter and Chen EAM potential as compared to the experimental values for silver. The parameters are: equilibrium lattice constant (a_0), bulk cohesive energy (E_{coh}), bulk modulus (B), cubic elastic constants (C_{11} , C_{12} , C_{44}), vacancy formation energy (ΔE_{vf}), diatomic molecule bond strength (D_e), and diatomic molecule bond length (R_e).

Property	Experimental	Voter and Chen
a_0 (Å)	4.09	4.09
E_{coh} (eV)	2.85	2.85
B (10^{12} erg cm ⁻³)	1.04	1.04
C_{11} (10^{12} erg cm ⁻³)	1.24	1.24
C_{12} (10^{12} erg cm ⁻³)	0.934	0.93
C_{44} (10^{12} erg cm ⁻³)	0.461	0.46
ΔE_{vf} (eV)	1.1	1.10
D_e (eV)	1.66	1.66
R_e (Å)	2.5	2.50

Data reproduced from^[59]

rhombic nanowires are each single crystal, while the pentagonal nanowire is comprised of five wedge-shaped single crystals (each with a <110> fiber texture) arranged in a pentagonal geometry.

The nanowires are created with atoms in positions corresponding to a bulk FCC crystal lattice. We do not consider periodic boundary conditions in any direction for the nanowires, thus atoms in proximity to free surfaces will have a tendency to contract in order to increase their effective electron density and thus decrease the energy of the system. To facilitate this contraction, the precursor to all simulations is conjugate gradient energy minimization. The nanowires are then dynamically equilibrated at 300 K using a Nosé-Hoover thermostat^[61, 62] for 100 ps. Free boundary conditions are prescribed during the dynamic equilibration to allow thermal expansion so that a stress-equilibrated state is maintained in the nanowire. The final step is to apply a tensile, displacement-controlled load to the nanowire until failure occurs. For this, two techniques are used: continuous dynamic and incremental dynamic loading.

In the continuous dynamic loading method, atoms in the nanowire are assigned a velocity in the axial, <110> direction according to a linearly varying velocity profile along the length of the nanowire. The velocity varies from zero at the fixed end of the nanowire to a maximum value at the free, resulting in a strain rate of 1×10^8 s⁻¹. This velocity profile mitigates loading-induced shock waves that are characteristic of a uniform velocity profile in MD simulations. While this strain rate is quite large in a classical sense, it is typical of MD simulations and is sufficiently below the strain rate at which precludes dislocation motion, which occurs on an extremely quick timeframe.^[28]

The incremental dynamic approach consists of a series of incremental displacements, during which each atom in the nanowire is displaced according to a linear profile. In the elastic regime (prior to permanent deformation), the nanowire is strained 0.45% of its length per increment, corresponding to approximately 10% of the yield strain per increment. Large displacements are allowable during

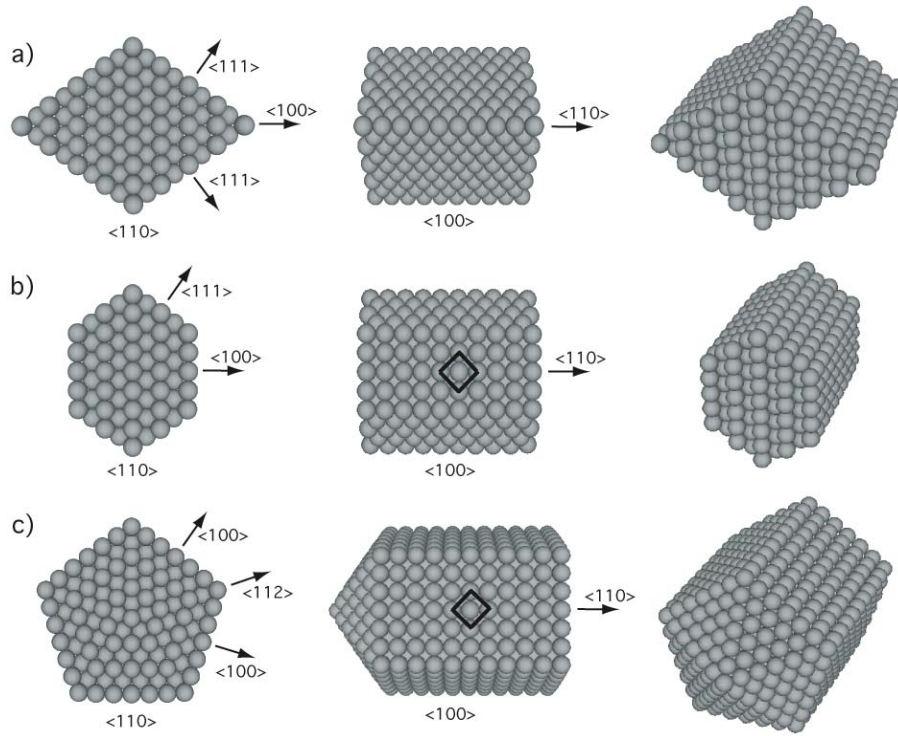


Figure 10. *Top-down* (a, b) and *bottom-up* (c) silver nanowires. Three views are shown for each wire type: cross-section (left), side view (middle), and three-dimensional perspective (right). The viewing direction is indicated below each image (left, middle). All wires have an FCC structure and are axially oriented in the $\langle 110 \rangle$ direction. The *top-down* nanowires have a rhombic (a) or truncated-rhombic (b) cross section. The rhombic wires have $\{111\}$ type lateral surfaces while the truncated-rhombic wires reveal $\{100\}$ facets in addition to the $\{111\}$ surfaces. The pentagonal nanowire (c) is representative of *bottom-up* fabrication, and may be considered as a multiply twinned nanowire. Five wedge shaped rods are separated by $\{111\}$ twin boundaries along the nanowire length, and are arranged in a pentagonal geometry. The lateral surfaces of the pentagonal wire are of a $\{100\}$ orientation, while the wire-ends expose low-energy, close-packed $\{111\}$ facets.

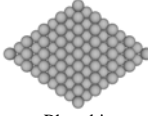
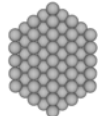
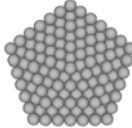
elastic deformation, since the material response is expected to be linear. As the elastic limit is approached, the displacements are reduced to 0.1% strain per increment. After each displacement, the ends of the wire are constrained from axial motion and the wire is dynamically equilibrated at 300 K for 100 ps. This incremental dynamic approach results in an effective strain rate of $1 \times 10^7 \text{ s}^{-7}$. During the equilibration, the axial stress saturates to a nearly constant value; this value is determined as a direct average of the stress over the latter 50 ps of equilibration. In both loading methods, the virial theorem is used for stress calculations and is averaged over the instantaneous *physical* volume of the nanowire.^[63, 64]

The detailed investigations of the deformation mechanisms for each nanowire (as presented in Figures 4, 6, and 8) were performed at 10K in order to reduce the contribution of thermal oscillations to the centrosymmetry values of the atoms. The continuous dynamic loading method was utilized at a strain rate of $1 \times 10^8 \text{ s}^{-1}$ for these simulations. No change in deformation mechanism was observed between the simulations at 10K and 300K.

We also performed simulations on the three geometries with diameters ranging from one to around twenty-five nanometers in order to investigate the effect of nanowire size on the tensile yield strength. For these simulations, where in some cases the system size exceeds 10^6 atoms, the continuous dynamic loading method was employed with a strain rate of

$1 \times 10^9 \text{ s}^{-1}$. Snapshots of the large nanowires after yield were observed to verify that no change in mechanism occurred. The dimensions and relative stability of all of the nanowires considered in this work are summarized in Table 2.

Table 2. Geometric parameters and relative stability of the simulated nanowires. The nanowire diameter (D) is the diameter of a circle with a cross sectional area equivalent to that of the nanowire being considered. The ratio of the nanowire length to the diameter was approximately 8 for all nanowires except the largest diameter of each geometry. For the large diameters, the aspect ratio was decreased to reduce the number of atoms in the system (N_A). The cohesive energy (E_{coh}) is a per-atom quantity and is a measure of the energetic stability of the nanowires. The nanowire configurations that are considered in detail are shown in bold.

Geometry	D (nm)	N_A	E_{coh} / E_{bulk}
 Rhombic	1.10	838	0.892
	2.20	4,982	0.940
	4.39	33,669	0.968
	7.13	135,229	0.980
	12.07	626,737	0.988
21.95	2,030,629	0.993	
 Truncated-Rhombic	0.95	638	0.881
	1.90	3,754	0.934
	3.80	25,285	0.965
	6.18	96,282	0.977
	10.46	470,142	0.987
19.01	1,471,694	0.992	
 Pentagonal	1.70	1,584	0.921
	2.56	6,117	0.946
	6.02	64,883	0.976
	8.61	181,136	0.983
	14.67	854,135	0.990
26.79	2,034,625	0.994	

- [1] N. Silvis-Cividjian, C. W. Hagen, P. Kruit, M. A. J. Van der Stam, H. B. Groen, *Applied Physics Letters* **2003**, 82, 3514.
- [2] S. Hu, A. Hamidi, S. Altmeyer, T. Koster, B. Spangenberg, H. Kurz, *Journal of Vacuum Science & Technology B* **1998**, 16, 2822.
- [3] N. Kramer, H. Birk, J. Jorritsma, C. Schonenberger, *Applied Physics Letters* **1995**, 66, 1325.
- [4] Y. Kondo, K. Takayanagi, *Physical Review Letters* **1997**, 79, 3455.
- [5] K. K. Caswell, C. M. Bender, C. J. Murphy, *Nano Letters* **2003**, 3, 667.
- [6] Y. Gao, P. Jiang, L. Song, L. F. Liu, X. Q. Yan, Z. Q. Zhou, D. F. Liu, J. X. Wang, H. J. Yuan, Z. X. Zhang, X. W. Zhao, X. Y. Dou, W. Y. Zhou, G. Wang, S. S. Xie, *Journal of Physics D-Applied Physics* **2005**, 38, 1061.
- [7] C. Y. Ni, P. A. Hassan, E. W. Kaler, *Langmuir* **2005**, 21, 3334.
- [8] G. Sauer, G. Brehm, S. Schneider, K. Nielsch, R. B. Wehrspohn, J. Choi, H. Hofmeister, U. Gosele, *Journal of Applied Physics* **2002**, 91, 3243.
- [9] T. Scheibel, R. Parthasarathy, G. Sawicki, X. M. Lin, H. Jaeger, S. L. Lindquist, *Proceedings of the National Academy of Sciences of the United States of America* **2003**, 100, 4527.
- [10] Y. G. Sun, B. Mayers, T. Herricks, Y. N. Xia, *Nano Letters* **2003**, 3, 955.
- [11] Y. G. Sun, Y. N. Xia, *Advanced Materials* **2002**, 14, 833.
- [12] N. R. Jana, L. Gearheart, C. J. Murphy, *Advanced Materials* **2001**, 13, 1389.
- [13] C. J. Murphy, N. R. Jana, *Advanced Materials* **2002**, 14, 80.
- [14] C. N. R. Rao, F. L. Deepak, G. Gundiah, A. Govindaraj, *Progress in Solid State Chemistry* **2003**, 31, 5.
- [15] Z. Y. Tang, N. A. Kotov, *Advanced Materials* **2005**, 17, 951.
- [16] Y. N. Xia, P. D. Yang, Y. G. Sun, Y. Y. Wu, B. Mayers, B. Gates, Y. D. Yin, F. Kim, Y. Q. Yan, *Advanced Materials* **2003**, 15, 353.
- [17] H. E. Boyer, *Atlas of Stress-Strain Curves*, ASM International, Metals Park, Ohio 44073, USA **1987**.
- [18] N. Agrait, G. Rubio, S. Vieira, *Physical Review Letters* **1995**, 74, 3995.
- [19] P. E. Marszalek, W. J. Greenleaf, H. B. Li, A. F. Oberhauser, J. M. Fernandez, *Proceedings of the National Academy of Sciences of the United States of America* **2000**, 97, 6282.
- [20] A. Stalder, U. Durig, *Journal of Vacuum Science & Technology B* **1996**, 14, 1259.
- [21] J. K. Diao, K. Gall, M. L. Dunn, *Nature Materials* **2003**, 2, 656.
- [22] J. K. Diao, K. Gall, M. L. Dunn, *Physical Review B* **2004**, 70, 075413.
- [23] J. K. Diao, K. Gall, M. L. Dunn, *Nano Letters* **2004**, 4, 1863.
- [24] J. K. Diao, K. Gall, M. L. Dunn, *Journal of the Mechanics and Physics of Solids* **2004**, 52, 1935.
- [25] J. K. Diao, K. Gall, M. L. Dunn, J. A. Zimmerman, *Acta Materialia* **2006**, 54, 643.
- [26] K. Gall, J. K. Diao, M. L. Dunn, *Nano Letters* **2004**, 4, 2431.
- [27] B. Hyde, H. D. Espinosa, D. Farkas, *Jom* **2005**, 57, 62.
- [28] W. Liang, M. Zhou, *Proceedings of the Institution of Mechanical Engineers Part C-Journal of Mechanical Engineering Science* **2004**, 218, 599.
- [29] W. W. Liang, M. Zhou, *Journal of Engineering Materials and Technology-Transactions of the Asme* **2005**, 127, 423.
- [30] W. W. Liang, M. Zhou, *Physical Review B* **2006**, 73, 115409.
- [31] W. W. Liang, M. Zhou, F. J. Ke, *Nano Letters* **2005**, 5, 2039.
- [32] H. S. Park, K. Gall, J. A. Zimmerman, *Physical Review Letters* **2005**, 95, 255504.
- [33] H. S. Park, C. J. Ji, *Acta Materialia* **2006**, 54, 2645.
- [34] H. S. Park, K. Gall, J. A. Zimmerman, *Journal of the Mechanics and Physics of Solids* **2006**, 54, 1862.
- [35] H. S. Park, J. A. Zimmerman, *Physical Review B* **2005**, 72, 054106.
- [36] J. A. Zimmerman, H. J. Gao, F. F. Abraham, *Modelling and Simulation in Materials Science and Engineering* **2000**, 8, 103.
- [37] T. Kizuka, *Physical Review Letters* **1998**, 81, 4448.
- [38] V. Rodrigues, T. Fuhrer, D. Ugarte, *Physical Review Letters* **2000**, 85, 4124.
- [39] G. E. Tommei, F. Baletto, R. Ferrando, R. Spadacini, A. Danani, *Physical Review B* **2004**, 69, 115426.

- [40] J. Bettini, V. Rodrigues, J. C. Gonzalez, D. Ugarte, *Applied Physics a-Materials Science & Processing* **2005**, *81*, 1513.
- [41] V. Rodrigues, J. Bettini, A. R. Rocha, L. G. C. Rego, D. Ugarte, *Physical Review B* **2002**, *65*, 153402.
- [42] H. Y. Chen, Y. Gao, H. C. Yu, H. R. Zhang, L. B. Liu, Y. G. Shi, H. F. Tian, S. S. Xie, J. Q. Li, *Micron* **2004**, *35*, 469.
- [43] H. Y. Chen, Y. Gao, H. R. Zhang, L. B. Liu, H. C. Yu, H. F. Tian, S. S. Xie, J. Q. Li, *Journal of Physical Chemistry B* **2004**, *108*, 12038.
- [44] Y. Gao, L. Song, P. Jiang, L. F. Liu, X. Q. Yan, Z. P. Zhou, D. F. Liu, J. X. Wang, H. J. Yuan, Z. X. Zhang, X. W. Zhao, X. Y. Dou, W. Y. Zhou, G. Wang, S. S. Xie, H. Y. Chen, J. Q. Li, *Journal of Crystal Growth* **2005**, *276*, 606.
- [45] H. Hofmeister, S. A. Nepijko, D. N. Ievlev, W. Schulze, G. Ertl, *Journal of Crystal Growth* **2002**, *234*, 773.
- [46] J. Reyes-Gasga, J. L. Elechiguerra, C. Liu, A. Camacho-Bragado, J. M. Montejano-Carrizales, M. J. Yacaman, *Journal of Crystal Growth* **2006**, *286*, 162.
- [47] C. Q. Chen, Y. Shi, Y. S. Zhang, J. Zhu, Y. J. Yan, *Physical Review Letters* **2006**, *96*, 075505.
- [48] S. Cuenot, C. Fretigny, S. Demoustier-Champagne, B. Nysten, *Physical Review B* **2004**, *69*, 165410.
- [49] G. Y. Jing, H. L. Duan, X. M. Sun, Z. S. Zhang, J. Xu, Y. D. Li, J. X. Wang, D. P. Yu, *Physical Review B* **2006**, *73*, 235409.
- [50] B. Wu, A. Heidelberg, J. J. Boland, J. E. Sader, X. M. Sun, Y. D. Li, *Nano Letters* **2006**, *6*, 468.
- [51] R. C. Cammarata, K. Sieradzki, *Physical Review Letters* **1989**, *62*, 2005.
- [52] F. Ding, H. Li, J. L. Wang, W. F. Shen, G. H. Wang, *Journal of Physics-Condensed Matter* **2002**, *14*, 113.
- [53] R. Dingreville, J. M. Qu, M. Cherkaoui, *Journal of the Mechanics and Physics of Solids* **2005**, *53*, 1827.
- [54] R. E. Miller, V. B. Shenoy, *Nanotechnology* **2000**, *11*, 139.
- [55] F. H. Streitz, R. C. Cammarata, K. Sieradzki, *Physical Review B* **1994**, *49*, 10699.
- [56] H. Y. Liang, M. Upmanyu, H. C. Huang, *Physical Review B* **2005**, *71*, 241403.
- [57] M. S. Daw, M. I. Baskes, *Physical Review B* **1984**, *29*, 6443.
- [58] M. S. Daw, S. M. Foiles, M. I. Baskes, *Materials Science Reports* **1993**, *9*, 251.
- [59] A. F. Voter, Los Alamos unclassified technical report LA-UR 93-3901.
- [60] Warp, <http://www.cs.sandia.gov/~sjplimp/lammps.html>.
- [61] W. G. Hoover, *Physical Review A* **1985**, *31*, 1695.
- [62] S. Nose, *Journal of Chemical Physics* **1984**, *81*, 511.
- [63] K. S. Cheung, S. Yip, *Journal of Applied Physics* **1991**, *70*, 5688.
- [64] M. Zhou, *Proceedings of the Royal Society of London Series a-Mathematical Physical and Engineering Sciences* **2003**, *459*, 2347.